NANO LETTERS

Letter

pubs.acs.org/NanoLett

Enhancing the Thermoelectric Figure of Merit by Low-Dimensional Electrical Transport in Phonon-Glass Crystals

Xue-Ya Mi,[†,#] Xiaoxiang Yu,[‡,#] Kai-Lun Yao,[†] Xiaoming Huang,[§] Nuo Yang,*[,‡,∥] and Jing-Tao Lü*[,†,⊥]

[†]School of Physics and Wuhan National High Magnetic Field Center, Huazhong University of Science and Technology, Wuhan 430074, P. R. China

[‡]Nano Interface Center for Energy (NICE), School of Energy and Power Engineering, Huazhong University of Science and Technology, Wuhan 430074, P. R. China

[§]School of Energy and Power Engineering, Huazhong University of Science and Technology, Wuhan 430074, P. R. China

[∥]State Key Laboratory of Coal Combustion, Huazhong University of Science and Technology, Wuhan 430074, P. R. China

[⊥]Beida Information Research, Tianjin 300457, P. R. China

Supporting Information

ABSTRACT: Low-dimensional electronic and glassy phononic transport are two important ingredients of highly efficient thermoelectric materials, from which two branches of thermoelectric research have emerged. One focuses on controlling electronic transport in the low dimension, while the other focuses on multiscale phonon engineering in the bulk. Recent work has benefited much from combining these two approaches, e.g., phonon engineering in low-dimensional materials. Here we propose to employ the low-dimensional electronic structure in bulk phonon-glass crystals as an alternative way to increase the thermoelectric efficiency. Through first-principles electronic structure calculations and classical molecular dynamics simulations, we show that the $\pi-\pi$-stacking bis(dithienothiophene) molecular crystal is a natural candidate for such an approach. This is determined by the nature of its chemical bonding. Without any optimization of the material parameters, we obtained a maximum room-temperature figure of merit, ZT, of 1.48 at optimal doping, thus validating our idea.

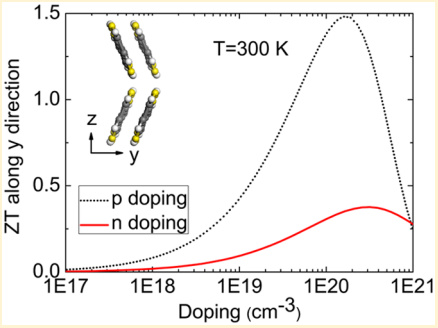

KEYWORDS: *Thermoelectric effect, molecular crystals, electronic structure calculations, molecular dynamics simulations*

The thermoelectric efficiency of a material is characterized by the dimensionless figure of merit, $ZT = \sigma S^2 T/(\kappa_e + \kappa_{ph})$, where S is the Seebeck coefficient, σ is the electrical conductivity, κ_e is the electron thermal conductivity, κ_{ph} is the phonon thermal conductivity, and T is the absolute temperature. The optimization of ZT is a highly nontrivial task, e.g., the electrical conductivity and the electron thermal conductivity are, in many cases, related by the Wiedemann−Franz law.

Different strategies have been proposed to increase the ZT value.[1−4] In their seminal work, Hicks and Dresselhaus proposed to increase S by utilizing the sharp change in the electrical density of states (DOS) in low-dimensional structures,[5−7] such as semiconductor quantum wells, quantum wires, quantum dots, and single-molecule devices.[3,4] Another approach is to search for or design electron-crystal−phonon-glass materials by phonon engineering (phononics).[8,9] The idea is to reduce the phonon thermal conductivity while keeping the electrical conductivity intact.[1] Recently, in a combination of these two approaches, phonon engineering is used in low-dimensional structures, such as silicon nanowires, to boost their ZT values.[10−14] A natural question then arises: Is it possible to do the opposite, i.e., to utilize low-dimensional electrical transport in bulk phonon-glass crystals? To show that this is indeed possible, we need to start from bulk materials with low thermal conductivity.

To date, the main focus of the thermoelectric research community has been inorganic semiconductor materials,[2,15] including Bi_2Te_3,[16] PbTe,[17] SiGe,[18] SnSe,[19] perovskites,[20] and Si.[21,22] Instead, we focus on organic semiconductors, especially molecular crystals, which have been intensively studied in the development of organic photovoltaic cells,[23] light-emitting diodes,[24] and field-effect transistors.[25,26] Currently, their thermoelectric properties have received more attention.[27−32] Compared with inorganic materials, organic thermoelectric materials have the advantages of being light-weight, flexible, cheap, and easy to process over large areas.[33] Because of the weak bonding between different molecules, organic molecular crystals have naturally low thermal conductivity. Recent experimental progress has resulted in an increase in ZT by several orders of magnitude, from 0.001−0.01[34,35] to 0.42.[36,37] Moreover, it is now possible to design and modulate the transport characteristics of organic structures.[31] Among them, $\pi-\pi$-stacking molecular crystals have proved their superior

Received: April 17, 2015
Revised: July 6, 2015
Published: July 7, 2015

DOI: 10.1021/acs.nanolett.5b01491
Nano Lett. 2015, 15, 5229−5234

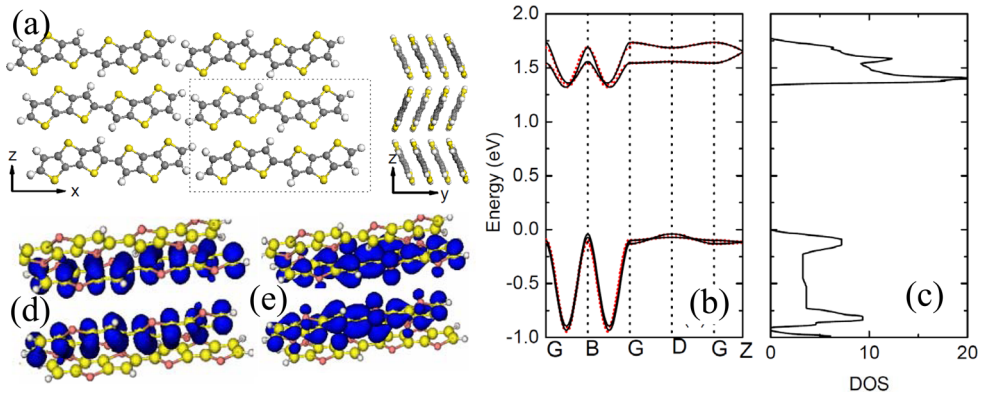

Figure 1. Lattice and DFT band structure. (a) Relaxed structure of the BDT crystal along different directions. The lattice vectors are a_1 = (16.82, 0.087, 0.015) Å, a_2 = (16.40, 3.85, 0.015) Å, and a_3 = (−2.08, −0.24, 10.68) Å. The y direction is approximately perpendicular to the molecular plane. (b, c) DFT band structure and density of states (DOS) of the BDT crystal. The energy zero is set to the top of the valence band. The reciprocal-space coordinates of high-symmetry points are G = (0, 0, 0), B = (−0.5, 0.5, 0), D = (0.5, 0.5, 0), and Z = (0, 0, 0.5) in units of the reciprocal lattice constants. The red dots represent the bands fitted using one-dimensional band dispersion, $\varepsilon \sim -2t\cos(kL_0)$, with t = −0.2, −0.2 eV for the two valence bands and −0.05, −0.08 eV for the two conduction bands (see the text for details). (d) Charge density distributions of the two nearly degenerate highest occupied molecular orbitals in one isolated unit cell. They are localized in each molecule and form the two valence bands in the lattice structure. (e) Corresponding lowest unoccupied molecular orbitals forming the conduction bands.

electronic transport properties in the development of organic field-effect transistors.[26] Interestingly, it has been shown that their electronic transport properties can be controlled by tuning the stacking angle and distance.[26,38]

Here, we focus on bis(dithienothiophene) molecular crystal (BDTMC), which has interesting electrochemical and optical properties.[39] As shown in Figure 1a, each dithienothiophene molecule possesses three fused thiophene rings, and they form a crystal structure through $\pi-\pi$ stacking. The way that small molecules stack together determines the structure and electronic properties of the organic crystal. Herringbone stacking is one of the common stacking structures, whose electronic band structure is normally two-dimensional as a result of $\pi-\pi$ stacking that extends in two dimensions. BDTMC favors coplanar stacking[40] and has high mobility.[28,40] As a result of the strong $\pi-\pi$ overlap along only one direction, it shows a quasi-one-dimensional (Q1D) band with a large band dispersion (Figure 1a,b). This Q1D band structure is different from the common two-dimensional bands in molecular crystals and appropriate for our study on thermoelectrics. Besides, its thermoelectric transport properties are under experimental investigation.[41]

On the basis of a general one-dimensional tight-binding model validated by density functional theory (DFT), we employed semiclassical Boltzmann transport theory to study its electronic transport properties. Meanwhile, the phonon thermal conductivity was calculated using classical molecular dynamics (MD) simulations. We show that Q1D electronic transport and phonon-glass-like thermal transport are realized at the same time in bulk BDTMC, which suggests a great thermoelectric potential for $\pi-\pi$-stacking organic molecular crystals.

Results and Discussion. *Electronic Structure.* The lattice and electronic structure of BDTMC were calculated using the Vienna Ab Initio Simulation Package (VASP).[42] The Perdew–Burke–Ernzerhof (PBE) version of the generalized gradient approximation (GGA) was used for the exchange–correlation functional.[43] The DFT-D2 method of Grimme was used to take into account the van der Waals (vdW) interactions between different molecules[44] (details are provided in section IA in the Supporting Information (SI)). Figure 1a shows the relaxed structure. It forms a triclinic Bravais lattice with two molecules within one primitive unit cell, shown in dashed lines. The conduction band (CB) and valence band (VB) structures and DOS are shown in Figure 1b,c. We observe a strong band dispersion along the y direction, G–B–G, compared with other directions. This indicates a large overlap of π orbitals between molecules along the y direction due to the small angle between y and the $\pi-\pi$ stacking (π) direction. The band structure along y was well-reproduced by a fit using the dispersion of a 1D tight-binding model (red dots). Model details are given in section II in the SI.

Because of a small electronic overlap between molecules in the same unit cell, the conduction and valence bands come in pairs, each mainly localized in one molecule. By comparing the charge distributions of the bands with the electronic states of the isolated molecule pair, we find that the VB and CB are simply formed by the highest occupied molecular orbitals (HOMOs) and lowest unoccupied molecular orbitals (LUMOs) of each molecule, respectively (Figure 1d,e). The strong anisotropy in the band dispersion suggests the formation of a Q1D band structure along the y direction. This is further supported by the van Hove-like high DOS near the band edges (Figure 1c). For a 1D system, the DOS is inversely proportional to the hopping element t. Thus, the DOS at the valence band edge is around one-third of the DOS at the conduction band edge. Hereafter, we focus on the electrical properties along the y direction.

The intrinsic transport mechanism in organic molecular crystals has been under active debate. Band and hopping models have been used to understand the experimental results.[45,46] It is commonly accepted that a bandlike model should be used if the intermolecular hopping element t is larger than or comparable to the molecule reorganization energy λ.[45,47] Following the method in ref 47, we obtained $\lambda \approx 0.18$ eV, which is comparable to t. Thus, we used the band model to study the transport along the y direction. This is also supported by the fact that the hopping model predicts a mobility that is 1 order of magnitude smaller than the experimental value in a similar molecular crystal.[48]

DOI: 10.1021/acs.nanolett.5b01491
Nano Lett. 2015, 15, 5229–5234

On the basis of the band structure obtained from VASP,[42] we used the BoltzTraP code[49] to calculate its contribution to the transport coefficients, e.g., $(\kappa_e + S^2\sigma T)/\tau$ and $S^2\sigma/\tau$, where τ is the constant relaxation time. The rigid-band approximation was used to relate the position of the Fermi level (E_f) to the electron and hole doping concentrations (Figure 2a). The weak

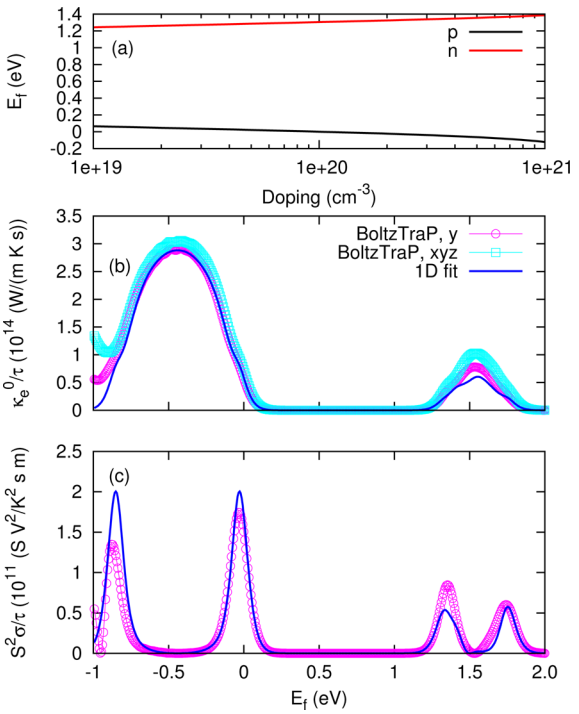

Figure 2. DFT plus BoltzTraP calculations and model fitting. (a) Position of the Fermi level (E_f) as a function of the electron (red) and hole (black) doping concentrations at T = 300 K. The weak dependence of the E_f on doping across three decades is characteristic of quasi-one-dimensional energy band. (b, c) Dependence of (b) $\kappa_e^0/\tau = (\kappa_e + S^2\sigma T)/\tau$ and (c) $S^2\sigma/\tau$ on E_f. The points are results from DFT plus BoltzTraP calculations, while the lines are from the 1D tight-binding model with the hopping element t fitted from the band structure in Figure 1b. In (b), *xyz* denotes the sum over all three directions, while *y* denotes the contribution from the *y* direction only. As can be seen, the contributions from *x* and *z* are negligible.

dependence of E_f on doping within 3 decades is due to the van Hove-like DOS at the band edges. Thus, similar to the Q1D structure, we expect a high Seebeck coefficient to show up in the bulk molecular crystal. The DFT result was further compared with a 1D model calculation using the parameters obtained from fitting the band structure (details are provided in section 1A in the SI). We found excellent agreement between the two approaches near the band edges (Figure 2b,c). This agreement validates the 1D model, which we will use in the following.

Electrical Transport. A common approach to obtain thermoelectric transport coefficients based on DFT plus BoltzTraP calculations is to use a constant τ. It is obtained from either fitting of the experiments or theoretical estimation. To estimate the relaxation time, we need to consider different types of carrier scattering processes. Defects and charge traps may scatter the carriers strongly and even invalidate the bandlike transport model used here. However, these scatterings are extrinsic and depend on the quality of the sample. Charged impurity scattering due to doping is another source of scattering. To take it into account, we should consider the screening of the charged impurity, which is a problem that deserves separate study. Here, we took into account only the intrinsic scattering mechanism, namely, the interaction of electrons with acoustic phonons, which is present independent of the quality of the sample. Because of the Q1D electronic structure, we used the Bardeen−Shockley deformation potential theory[50,51] to go beyond the constant-τ approach by taking into account the k dependence of $\tau(k)$ (section II in the SI):

$$\frac{1}{\tau(k)} \approx \frac{k_B T D^2}{\hbar^2 C |v_k|} \tag{1}$$

in which k_B is the Boltzmann constant; T is the absolute temperature; $C = L_0^{-1}\,\partial^2 E/\partial \Delta L^2$ is the 1D elastic constant, where $\Delta L = \delta L/L_0$; and $D = \Delta E/\Delta L$ is the deformation potential constant, where ΔE is the energy shift of the valence or conduction band edge (section IB in the SI). This makes our approach different from the common BoltzTraP calculation and much closer to the real situation. The relevant transport coefficients κ_e and σ are shown in Figure 3a,b, respectively. We see better transport performance of the holes, which can be attributed to their larger hopping element t, leading to a larger group velocity (section II in the SI). Moreover, a strong deviation from the Wiedemann−Franz law can be observed in Figure 3c, which is typical for band edges or low-dimensional structures. The smaller value of $\kappa_e/(T\sigma) < L$ indicates reduced electron thermal conductivity and good thermoelectric performance.

Phonon Transport. To get ZT, we also need the phonon thermal conductivity κ_{ph}, which was calculated by equilibrium MD simulations using LAMMPS[52] (details are given in section III in the SI). The following results were obtained from a simulation cell of 4 × 6 × 4 unit cells in the *x*, *y*, and *z* directions, respectively, to overcome the finite size effect (section III in the SI). As shown in Figure 4, the thermal conductivity of BDTMC exhibits a very weak temperature dependence over the temperature range considered (100−350 K). This weak temperature dependence is normally observed at the high-temperature limit, which is well within the validity of classical MD simulations. We obtained a value of 0.34 ± 0.02 W m^{-1} K^{-1} at 300 K, which falls into the common range of 0.1−1 W m^{-1} K^{-1} for organic molecular crystals.[29−31]

The low thermal conductivity originates from the weak intermolecular bonding of vdW nature, in contrast to the strong intramolecular valence bonding. Different kinds of bonds result in very different frequency/time scales of inter- and intramolecular dynamics. The thermal conductivity of the molecular crystal is dominated by the low-frequency intermolecular vibrations. Their frequency mismatch with the intramolecular vibrations prevents efficient heat transport between molecules, which is good for thermoelectric performance. That is, most of the energy is localized inside each molecule instead of being transferred to other molecules. This can be seen from the large overshot of κ_{ph} as a function of correlation time (Figure S4 in the SI).

Thermoelectric Performance. We are now in a position to evaluate the thermoelectric figure of merit ZT. As shown in Figure 3d, we obtained optimal room-temperature ZT values of 0.38 at an electron doping of ∼3.2 × 10^{20} cm^{-3} and 1.48 at a hole doping of ∼1.57 × 10^{20} cm^{-3}. The corresponding Seebeck coefficients are −199 μV/K for electrons and 266 μV/K for

DOI: 10.1021/acs.nanolett.5b01491
Nano Lett. 2015, 15, 5229−5234

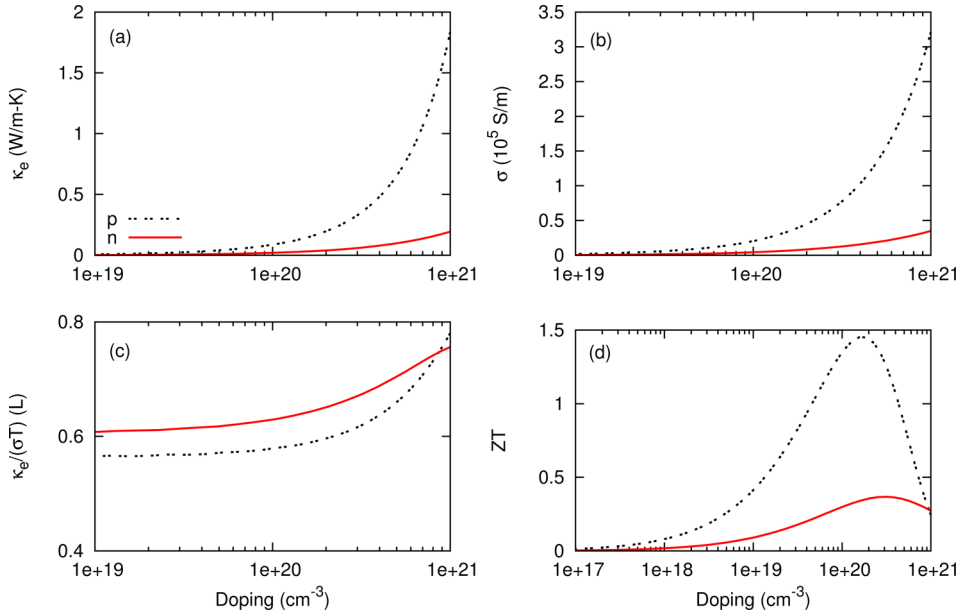

Figure 3. Thermoelectric transport coefficients at 300 K. (a, b) Electron thermal conductivity κ_e and electrical conductivity σ as functions of electron (n) and hole (p) doping concentrations. (c) $\kappa_e/(\sigma T)$ as a function of doping concentration. $\kappa_e/(\sigma T)$ is given in units of the Lorentz number $L = \pi^2 k_B^2/(3e^2)$, such that the Wiedemann–Franz law corresponds to $\kappa_e/(\sigma T) = L$. (d) ZT as a function of doping concentration.

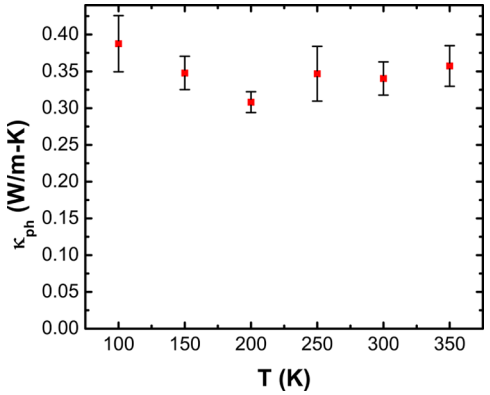

Figure 4. Phonon thermal conductivity as a function of temperature obtained from the classical molecular dynamics simulations.

holes. The electron and hole mobilities at optimal doping are ~2.4 and ~12.8 $cm^2\ V^{-1}\ s^{-1}$, respectively. These results are summarized in Table 1. The following facts are note-worthy: (1) Although doping of organic semiconductors is still challenging in experiments, the optimal doping level we obtained here has been achieved in pentacene experimentally.[53] (2) A much higher carrier mobility has been experimentally observed in C8-BTBT.[54] (3) Although the optimal electrical conductivity we obtained here has not been realized to date (the highest experimental value that has been achieved[31] is ~11 000 S/m), there is no fundamental difficulty in realizing both (1) and (2) in the same material. (4) On the other hand, a recent study showed that it is possible to reduce the optimal doping by increasing the carrier mobility.[55] Finally, in Figure 5,

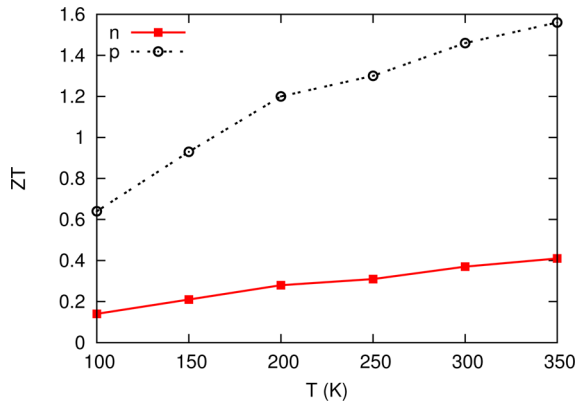

Figure 5. Temperature dependence of ZT at optimal doping.

we have plotted the temperature dependence of ZT. It can be seen that ZT shows an approximately linear dependence on T. We have checked that ZT saturates at higher T (Figure S6 in the SI). Since bandlike transport at high T is questionable, we did not show it here. The ZT value is promising over a wide temperature range (100–350 K).

The Q1D electrical transport and low phonon thermal conductivity obtained here originate from the chemical nature of the intermolecular bonding. In our calculations, the conduction and valence band structures of BDTMC were

Table 1. Summary of Important Parameters and Results for the Conduction Band (CB) and Valence Band (VB)[a]

	t (eV)	m^* (m_0)	D (eV)	n (10^{20} cm^{-3})	ZT	μ ($cm^2\ V^{-1}\ s^{-1}$)	S (μV/K)	κ_e ($W\ m^{-1}\ K^{-1}$)
CB	0.05 (0.08)	4.27	−6.67	3.19	0.38	2.4	−199	0.06
VB	0.2	−1.5	−8.55	1.57	1.48	12.8	266	0.15

[a] t is the hopping element in the 1D model, m^* is the effective mass, D is the deformation potential, and μ and S are the mobility and Seebeck coefficient, respectively, at optimal doping (n).

DOI: 10.1021/acs.nanolett.5b01491
Nano Lett. 2015, 15, 5229–5234

determined by only one parameter, t, reflecting the strength of the $\pi-\pi$ vdW bonding. By comparing the results for the CB and VB, we deduce that stronger bonding (and thus larger t) results in better thermoelectric performance.

Our results, together with recent developments in chemical control of the stacking angle and distance,[26,38] point out a possible way to further enhance the thermoelectric performance by chemical or strain engineering of the $\pi-\pi$ overlap integral. DFT calculations confirmed this idea. Within a lattice strain of 5%, we can achieve a more than 20% change in t (Figure S2 in the SI).

Before closing, we should mention that as the doping concentration is increased, the impurity scattering rate also increases proportionally to the doping concentration, resulting in a decrease in σ and κ_e. However, their ratio should not change much. Since $ZT = S^2/[\kappa_e/(\sigma T) + \kappa_{ph}/(\sigma T)]$, we expect the ZT to be smaller after the impurity scattering is included, but to include it quantitatively, we need to consider the screening of charged impurities, which depends on the dimension and dispersion of the electronic band structure. Since the main idea of this work does not rely on these details, we leave them to future study.

Conclusions. We have proposed a novel approach to search for highly efficient thermoelectric materials, namely, to explore or engineer low-dimensional electronic structure in phonon-glass bulk crystals. Through atomistic simulations, we have shown that $\pi-\pi$-stacking molecular crystals are particularly suitable for such an approach. Both low phonon thermal conductivity and 1D electronic structure originate from the $\pi-\pi$ bonding. Besides proving the principle, our results also show the promising potential of $\pi-\pi$-stacking organic crystals as efficient thermoelectric materials. Although we considered only organic crystals in this work, the idea should be equally applicable to inorganic materials. Indeed, during the preparation of this work we became aware of a recent study exploring a similar idea with inorganic compounds.[56]

■ ASSOCIATED CONTENT

Supporting Information

Details of VASP band structure calculations, molecular dynamics simulations, and the one-dimensional model theory. The Supporting Information is available free of charge on the ACS Publications website at DOI: 10.1021/acs.nanolett.5b01491.

■ AUTHOR INFORMATION

Corresponding Authors

*E-mail: nuo@hust.edu.cn.

*E-mail: jtlu@hust.edu.cn.

Author Contributions

#X.-Y.M. and X.Y. contributed equally to the work.

Notes

The authors declare no competing financial interest.

■ ACKNOWLEDGMENTS

J.-T.L. acknowledges stimulating discussions with members of the Danish−Chinese Center for Molecular Nanoelectronics, from which the idea was initialized. J.-T.L. was supported by the National Natural Science Foundation of China (Grants 11304107 and 61371015). N.Y. was supported by the National Natural Science Foundation of China (Grant 11204216) and the Self-Innovation Foundation of HUST (Grant 2014TS115). The authors thank the National Supercomputing Center in Tianjin (NSCC-TJ) and Shanghai and the High Performance Computing Center Experimental Testbed in SCTS/CGCL for providing help in computations.

■ REFERENCES

(1) Snyder, G. J.; Toberer, E. S. *Nat. Mater.* **2008**, *7*, 105−114.
(2) Chen, G.; Dresselhaus, M. S.; Dresselhaus, G.; Fleurial, J.-P.; Caillat, T. *Int. Mater. Rev.* **2003**, *48*, 45−66.
(3) Dresselhaus, M. S.; Chen, G.; Tang, M. Y.; Yang, R. G.; Lee, H.; Wang, D. Z.; Ren, Z. F.; Fleurial, J. P.; Gogna, P. *Adv. Mater.* **2007**, *19*, 1043−1053.
(4) Dubi, Y.; Di Ventra, M. *Rev. Mod. Phys.* **2011**, *83*, 131−155.
(5) Hicks, L. D.; Dresselhaus, M. S. *Phys. Rev. B: Condens. Matter Mater. Phys.* **1993**, *47*, 12727−12731.
(6) Hicks, L. D.; Dresselhaus, M. S. *Phys. Rev. B: Condens. Matter Mater. Phys.* **1993**, *47*, 16631−16634.
(7) Mahan, G. D.; Sofo, J. O. *Proc. Natl. Acad. Sci. U. S. A.* **1996**, *93*, 7436−7439.
(8) Li, N.; Ren, J.; Wang, L.; Zhang, G.; Hänggi, P.; Li, B. *Rev. Mod. Phys.* **2012**, *84*, 1045−1066.
(9) Wang, J.-S.; Wang, J.; Lü, J. T. *Eur. Phys. J. B* **2008**, *62*, 381−404.
(10) Hochbaum, A. I.; Chen, R.; Delgado, R. D.; Liang, W.; Garnett, E. C.; Najarian, M.; Majumdar, A.; Yang, P. *Nature* **2008**, *451*, 163−167.
(11) Boukai, A. I.; Bunimovich, Y.; Tahir-Kheli, J.; Yu, J.; Goddard, W. A., III; Heath, J. R. *Nature* **2008**, *451*, 168−171.
(12) Markussen, T.; Jauho, A.; Brandbyge, M. *Phys. Rev. Lett.* **2009**, *103*, 055502.
(13) Brovman, Y. M.; Small, J. P.; Hu, Y.; Fang, Y.; Lieber, C. M.; Kim, P. 2013, arXiv:cond-mat/1307.0249. arXiv.org e-Print archive. http://arxiv.org/abs/1307.0249 (accessed April 17, 2015).
(14) Kiršanskas, G.; Li, Q.; Flensberg, K.; Solomon, G. C.; Leijnse, M. *Appl. Phys. Lett.* **2014**, *105*, 233102.
(15) Zhao, L.-D.; Dravid, V. P.; Kanatzidis, M. G. *Energy Environ. Sci.* **2014**, *7*, 251−268.
(16) Poudel, B.; Hao, Q.; Ma, Y.; Lan, Y.; Minnich, A.; Yu, B.; Yan, X.; Wang, D.; Muto, A.; Vashaee, D.; Chen, X.; Liu, J.; Dresselhaus, M. S.; Chen, G.; Ren, Z. *Science* **2008**, *320*, 634−638.
(17) Biswas, K.; He, J.; Zhang, Q.; Wang, G.; Uher, C.; Dravid, V. P.; Kanatzidis, M. G *Nat. Chem.* **2011**, *3*, 160−166.
(18) Yu, B.; Zebarjadi, M.; Wang, H.; Lukas, K.; Wang, H.; Wang, D.; Opeil, C.; Dresselhaus, M.; Chen, G.; Ren, Z. *Nano Lett.* **2012**, *12*, 2077−2082.
(19) Zhao, L.-D.; Lo, S.-H.; Zhang, Y.; Sun, H.; Tan, G.; Uher, C.; Wolverton, C.; Dravid, V. P.; Kanatzidis, M. G. *Nature* **2014**, *508*, 373−377.
(20) Koumoto, K.; Wang, Y.; Zhang, R.; Kosuga, A.; Funahashi, R. *Annu. Rev. Mater. Res.* **2010**, *40*, 363.
(21) Jiang, J.-W.; Yang, N.; Wang, B.-S.; Rabczuk, T. *Nano Lett.* **2013**, *13*, 1670−1674.
(22) Yang, L.; Yang, N.; Li, B. *Nano Lett.* **2014**, *14*, 1734−1738.
(23) Parida, B.; Iniyan, S.; Goic, R. *Renewable Sustainable Energy Rev.* **2011**, *15*, 1625−1636.
(24) Kalyani, N. T.; Dhoble, S. *Renewable Sustainable Energy Rev.* **2012**, *16*, 2696−2723.
(25) Dimitrakopoulos, C.; Malenfant, P. *Adv. Mater.* **2002**, *14*, 99−117.
(26) Dong, H.; Fu, X.; Liu, J.; Wang, Z.; Hu, W. *Adv. Mater.* **2013**, *25*, 6158−6183.
(27) Zhang, L.; Tan, L.; Hu, W.; Wang, Z. *J. Mater. Chem.* **2009**, *19*, 8216−8222.
(28) Zhang, L.; Tan, L.; Wang, Z.; Hu, W.; Zhu, D. *Chem. Mater.* **2009**, *21*, 1993−1999.
(29) Wang, D.; Shi, W.; Chen, J.; Xi, J.; Shuai, Z. *Phys. Chem. Chem. Phys.* **2012**, *14*, 16505−16520.
(30) Chen, J.; Wang, D.; Shuai, Z. *J. Chem. Theory Comput.* **2012**, *8*, 3338−3347.

DOI: 10.1021/acs.nanolett.5b01491
Nano Lett. 2015, 15, 5229−5234

(31) Zhang, Q.; Sun, Y.; Xu, W.; Zhu, D. *Adv. Mater.* **2014**, *26*, 6829−6851.
(32) Casian, A. I.; Sanduleac, I. I. *J. Thermoelectr.* **2013**, No. 3, 11−20.
(33) Leclerc, M.; Najari, A. *Nat. Mater.* **2011**, *10*, 409−410.
(34) Mateeva, N.; Niculescu, H.; Schlenoff, J.; Testardi, L. R. *J. Appl. Phys.* **1998**, *83*, 3111−3117.
(35) Pfeiffer, M.; Beyer, A.; Fritz, T.; Leo, K. *Appl. Phys. Lett.* **1998**, *73*, 3202−3204.
(36) Yue, R.; Xu, J. *Synth. Met.* **2012**, *162*, 912−917.
(37) Kim, G.-H.; Shao, L.; Zhang, K.; Pipe, K. P. *Nat. Mater.* **2013**, *12*, 719−723.
(38) Giri, G.; Verploegen, E.; Mannsfeld, S. C. B.; Atahan-Evrenk, S.; Kim, D. H.; Lee, S. Y.; Becerril, H. A.; Aspuru-Guzik, A.; Toney, M. F.; Bao, Z. *Nature* **2011**, *480*, 504−508.
(39) Ozturk, T.; Ertas, E.; Mert, O. *Tetrahedron* **2005**, *61*, 11055−11077.
(40) Sirringhaus, H.; Friend, R. H.; Li, X. C.; Moratti, S. C.; Holmes, A. B.; Feeder, N. *Appl. Phys. Lett.* **1997**, *71*, 3871−3873.
(41) Jiang, X.; Wei, Z.; Hu, W.; Qiu, X. Private communications.
(42) Kresse, G.; Furthmüller, J. *Comput. Mater. Sci.* **1996**, *6*, 15−50.
(43) Perdew, J.; Burke, K.; Ernzerhof, M. *Phys. Rev. Lett.* **1996**, *77*, 3865−3868.
(44) Grimme, S. *J. Comput. Chem.* **2004**, *25*, 1463−1473.
(45) Coropceanu, V.; Cornil, J.; da Silva Filho, D. A.; Olivier, Y.; Silbey, R.; Brédas, J.-L. *Chem. Rev.* **2007**, *107*, 926−952.
(46) Pernstich, K. P.; Rössner, B.; Batlogg, B. *Nat. Mater.* **2008**, *7*, 321−325.
(47) Kobayashi, H.; Kobayashi, N.; Hosoi, S.; Koshitani, N.; Murakami, D.; Shirasawa, R.; Kudo, Y.; Hobara, D.; Tokita, Y.; Itabashi, M. *J. Chem. Phys.* **2013**, *139*, 014707.
(48) Tan, L.; Zhang, L.; Jiang, X.; Yang, X.; Wang, L.; Wang, Z.; Li, L.; Hu, W.; Shuai, Z.; Li, L.; Zhu, D. *Adv. Funct. Mater.* **2009**, *19*, 272−276.
(49) Madsen, G. K. H.; Singh, D. J. *Comput. Phys. Commun.* **2006**, *175*, 67−71.
(50) Bardeen, J.; Shockley, W. *Phys. Rev.* **1950**, *80*, 72−80.
(51) Beleznay, F. B.; Bogár, F.; Ladik, J. *J. Chem. Phys.* **2003**, *119*, 5690−5695.
(52) Plimpton, S. *J. Comput. Phys.* **1995**, *117*, 1−19.
(53) Hayashi, K.; Shinano, T.; Miyazaki, Y.; Kajitani, T. *J. Appl. Phys.* **2011**, *109*, 023712.
(54) Yuan, Y.; Giri, G.; Ayzner, A. L.; Zoombelt, A. P.; Mannsfeld, S. C. B.; Chen, J.; Nordlund, D.; Toney, M. F.; Huang, J.; Bao, Z. *Nat. Commun.* **2014**, *5*, 3005.
(55) Shi, W.; Chen, J.; Xi, J.; Wang, D.; Shuai, Z. *Chem. Mater.* **2014**, *26*, 2669−2677.
(56) Bilc, D. I.; Hautier, G.; Waroquiers, D.; Rignanese, G.-M.; Ghosez, P. *Phys. Rev. Lett.* **2015**, *114*, 136601.

DOI: 10.1021/acs.nanolett.5b01491
Nano Lett. 2015, 15, 5229−5234

Supporting Information for "Enhancing thermoelectric figure-of-merit by low-dimensional electrical transport in phonon-glass crystals"

Xue-Ya Mi,[†,⊥] Xiaoxiang Yu,[‡,⊥] Kai-Lun Yao,[†] Xiaoming Huang,[‡] Nuo Yang,[*,¶,§] and Jing-Tao Lü[*,†,‖]

†*School of Physics and Wuhan National High Magnetic Field Center, Huazhong University of Science and Technology, Wuhan 430074, P. R. China*

‡*School of Energy and Power Engineering, Huazhong University of Science and Technology, Wuhan 430074, P. R. China*

¶*Nano Interface Center for Energy (NICE), School of Energy and Power Engineering, Huazhong University of Science and Technology, Wuhan 430074, P. R. China*

§*State Key Laboratory of Coal Combustion, Huazhong University of Science and Technology, Wuhan 430074, China*

‖*Beida Information Research, Tianjin 300457, China*

⊥*These authors contributed equally to the work*

E-mail: nuo@hust.edu.cn; jtlu@hust.edu.cn

I. DFT calculation

A. Electronic structure

The electronic structure is calculated using VASP, which uses plane wave basis set, and PAW pseudopotentials.[1] The Perdew-Burke-Ernzerhof (PBE) version of generalized gradient approximation (GGA) is used for the exchange-correlation potential.[2] The DFT-D2 method of Grimme is used to take into account the van der Waals (VDW) interactions between different molecules.[3] The cutoff energy of the plane wave expansion is set to 400 eV. For the geometry optimization, the reciprocal space is sampled by a $4 \times 4 \times 4$ Monkhorst-Pack k-meshes. The convergence criteria for the DFT self-consistent loop is set as 10^{-4} eV. The atomic positions are fully relaxed until the force on all atoms is less than 0.05 eV/Å. In the band structure and DOS calculation, a finer mesh of $8 \times 8 \times 8$ is used. We note that GGA without VDW or LDA calculation gives slightly different unit cells. But the final results are not sensitive to these small changes. Thus, we only show results from GGA plus VDW calculation.

The electronic structure contribution to the thermoelectric transport properties are calculated using the BoltzTraP code.[4] It is based on the semi-classical Boltzmann transport theory in the constant relaxation time approximation. The DFT result is fitted using a 1D tight-binding model [Fig. 2]. Based on their excellent agreement, further calculations are performed using the 1D model. Details of the 1D model are given in Sec. II.

B. The deformation potential and elastic constant

To estimate the deformation potential D and the elastic constant C, we performed VASP calculation by changing the lattice constant along y direction. From these calculations, we got $C = \partial^2 E/(L_0 \partial \Delta L^2)$ with $\Delta L = \delta L/L_0$, and $D = \Delta E/\Delta L$ with ΔE the energy shift of the valence or conduction band edge. We have assumed that the energy of core electrons, used as the energy reference, does not change with the deformation. The calculated result is

shown in Fig. S1(a), from which a linear fit gives $D = -6.67$ and -8.55 eV for electrons and holes, respectively. The total energy with respect to the dilatation is shown in Fig. S1(b). Fitting it with a parabola gives $C = 42.2$ eV/Å.

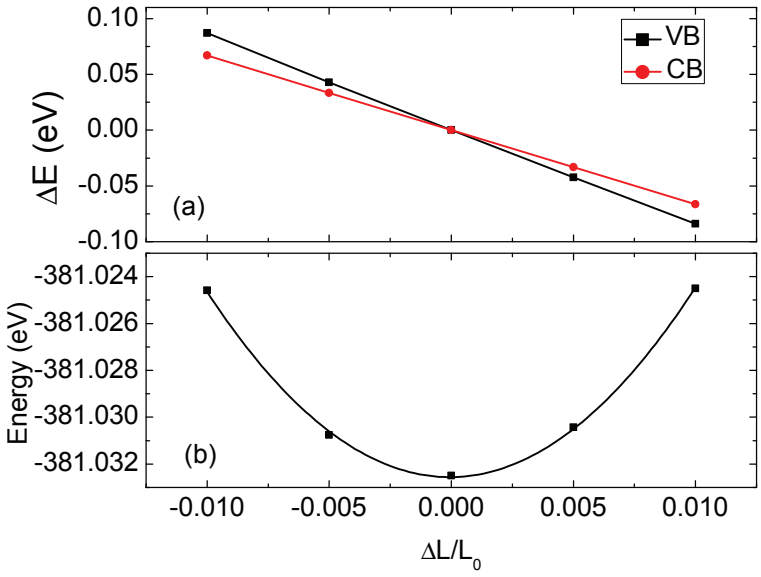

Figure S1: (a) The conduction (red) and valence (black) band edge shift as a function of the lattice dilatation along y direction. (b) The total energy of a unit cell as a function of lattice dilatation.

C. Strain tuning of the hopping matrix element

Inspired by recent experimental progress,[5] we calculated the effect of strain on the electronic band structure. Figure S2 shows the intermolecular hopping element t fitted from the 1D model as a function of the lattice deformation along y direction. We can achieve more than 20% change of t. This suggests that strain engineering could be used to enhance the thermoelectric transport performance of the molecular crystal.

II. Model theory

We fit the electronic band structure from VASP calculation using a 1D tight-binding model. We set the energy zero to the bottom of the band, e.g., considering conduction band. The

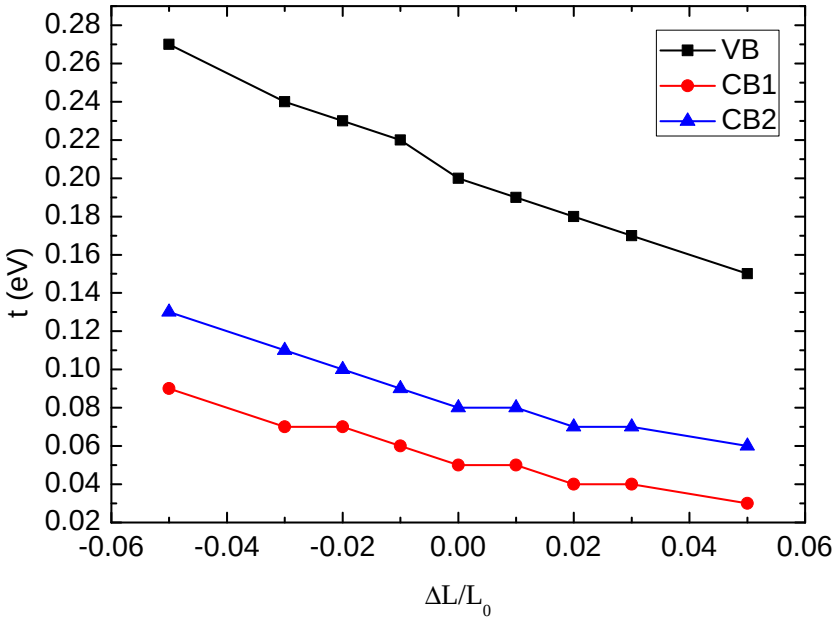

Figure S2: The intermolecular hopping element t fitted from the 1D model as a function of the lattice deformation along y direction.

energy dispersion is

$$\varepsilon(k) = 2t\big[1 - \cos(kL_0)\big]. \tag{S1}$$

Here, L_0 is the lattice constant, t is the nearest neighbour hopping element, and k is the electron wavevector. The group velocity of state k is then

$$v(k) = \frac{2L_0}{\hbar} t \sin(kL_0). \tag{S2}$$

Within the constant relaxation time approximation, we get

$$\frac{\sigma}{\tau} = \frac{2se^2 tL_0}{A_0 \pi \hbar^2} \int_0^{4t} \sqrt{1 - \left(1 - \frac{\varepsilon}{2t}\right)^2} \left(-\frac{\partial f}{\partial \varepsilon}\right) d\varepsilon. \tag{S3}$$

This expression is used to fit the DFT plus BoltzTraP calculation in Fig. 2. We find excellent agreement between the two approaches near the band edges [Fig. 2(b-c)]. The hopping element t is obtained by fitting the VASP electronic structure in Fig. 1(b) to Eq. (S1), $s = 2$

accounts for the spin degeneracy, e is the absolute magnitude of electron charge, $A_0 = 89.3$ Å^2 is the single molecular cross-section area normal to the y direction, $\hbar$ is the reduced Planck constant, and $f(\varepsilon, T) = \left[1 + \exp\left(\frac{\varepsilon-\mu}{k_B T}\right)\right]^{-1}$ is the Fermi distribution, with μ the chemical potential, T the temperature.

Using the Bardeen-Shockley deformation potential theory,[6] the k-dependent relaxation time is[7]

$$\frac{1}{\tau(k)} \approx \frac{k_B T D^2}{\hbar^2 C |v_k|}. \tag{S4}$$

Here, D is the deformation potential, C is the elastic constant, k_B is the Boltzmann constant. Using Eq. (S4) we can define the transport function

$$\mathcal{L}^{(n)} = \Delta \int_0^{4t} (\varepsilon - \mu)^n \left[1 - \left(1 - \frac{\varepsilon}{2t}\right)^2\right] \left(-\frac{\partial f}{\partial \varepsilon}\right) d\varepsilon \tag{S5}$$

with

$$\Delta = \frac{4 s e^2 t^2 L_0^2 C}{A_0 \pi \hbar k_B T D^2}. \tag{S6}$$

The thermoelectric transport coefficients in Fig. 3 are obtained from

$$\sigma = \mathcal{L}^{(0)}, \tag{S7}$$

$$S = -\frac{\mathcal{L}^{(1)}}{eT\mathcal{L}^{(0)}}, \tag{S8}$$

$$\kappa_{\mathrm{e}} = \frac{1}{e^2 T}\left(\mathcal{L}^{(2)} - \frac{{\mathcal{L}^{(1)}}^2}{\mathcal{L}^{(0)}}\right) = \frac{\mathcal{L}^{(2)}}{e^2 T} - S^2 \sigma T. \tag{S9}$$

From Eq. (S9), we see that a large Seebeck coefficient reduces κ_{e} and leads to violation of the Wiedemann-Franz law.

Now we want to understand why larger hopping element t gives larger ZT. Since this is true even at low temperature, we will limit ourselves to this situation, e.g., $\mu \gg k_B T$, such that the Summerfeld expansion is valid. When the effective mass approximation is valid,

e.g., not too far from the band edge, we get

$$\mathcal{L}^{(n)} \approx \frac{4se^2\hbar C}{A_0 m^* k_B T D^2} \int_0^{4t} (\varepsilon-\mu)^n \varepsilon \left(-\frac{\partial f}{\partial \varepsilon}\right) \frac{d\varepsilon}{2\pi}. \tag{S10}$$

Using the Summerfeld expansion, we find

$$\mathcal{L}^{(0)} \approx \frac{2se^2\hbar C\mu}{A_0\pi m^* k_B T D^2} = \frac{3\mu}{\pi^2 k_B^2 T^2}\mathcal{L}^{(1)}, \quad \mathcal{L}^{(1)} \approx \frac{2se^2\hbar\pi C k_B T}{3A_0 m^* D^2}, \quad \mathcal{L}^{(2)} \approx \mu\mathcal{L}^{(1)}, \tag{S11}$$

where we have used

$$\int_0^{+\infty} \frac{x^2 e^x}{(1+e^x)^2} dx = \frac{\pi^2}{6}. \tag{S12}$$

The thermoelectric figure of merit can be written as

$$ZT = \frac{S^2}{\frac{\kappa_e}{\sigma T} + \frac{\kappa_{ph}}{\sigma T}}. \tag{S13}$$

We notice that, within this 1D model, both S^2 and $\frac{\kappa_e}{\sigma T}$ are not sensitive to t (see Fig. 3(c) and Eqs. (S7-S9)). Thus, the only t dependence comes from σ in the second term in the denorminator. That means, the larger t is, the higher ZT one obtains. This explains why the holes show better performance than electrons in Fig. 5. And increasing the overlap t may lead to better thermoelectric performance.

III. MD simulation details and results

A. Atomic potential

To describe the atom bond and angle interactions, harmonic expressions are employed to represent the bond and angle potential. The VDW interactions between molecules are expressed

as 6-12 potential

$$E_{\text{total}} = \sum_{\text{bonds}} K_r(r - r_{\text{eq}})^2 + \sum_{\text{angles}} K_\theta(\theta - \theta_{\text{eq}})^2 + \sum_{\text{VDW}} \varepsilon_{ij} \left[\left(\frac{\sigma_{ij}}{r_{ij}} \right)^{12} - 2 \left(\frac{\sigma_{ij}}{r_{ij}} \right)^{6} \right]. \quad \text{(S14)}$$

The parameters of bond, angle, VDW are taken from Ref.,[8] and listed in Table S1. For the convenience of the MD simulation, we use a four-molecule unit cell, which is twice as large as the VASP calculation.

Table S1: The parameters of bond, angle, VDW in potential functions. The σ and ε used in Eq. (S14) for an interaction of atom i and atom j is $\sigma_{ij} = \sigma_i + \sigma_j$ and $\varepsilon_{ij} = \sqrt{\varepsilon_i \cdot \varepsilon_j}$, respectively.

Bond Parameters		
bond	K_r (kcal/(mol· Å^2))	r_{eq} (Å)
S-C	227.0	1.181
C-C	317.0	1.507
C-H	367.0	1.080
C=C	570.0	1.350
Angle Parameters		
angle	K_θ (kcal/(mol· radian^2))	θ_{eq} (degrees)
S-C-C	50.0	131.10
S-C=C	50.0	114.70
S-C-H	50.0	109.50
C-S-C	62.0	98.90
C-C=C	63.0	117.00
C-C-H	35.0	120.00
C=C-H	35.0	119.70
VDW Parameters		
atom type	ε (kcal/mol)	σ (Å)
S	0.2500	2.0000
C	0.0860	1.9080
H	0.0150	1.4590

B. Method

The Green-Kubo formula relates the ensemble average of the heat flux ($\vec{J}$) auto-correlation to the thermal conductivity ($\kappa_{\rm ph}$). The heat current is defined as

$$\vec{J} = \frac{1}{V}\left[\sum_i e_i \vec{v}_i + \frac{1}{2}\sum_{i<j}\left(\vec{f}_{ij}\cdot(\vec{v}_i+\vec{v}_j)\right)\vec{x}_{ij}\right]. \tag{S15}$$

The thermal conductivity is derived from the Green-Kubo equation as

$$\kappa_{\rm ph} = \frac{V}{3k_B T^2}\int_0^{\tau_0}\langle \vec{J}(0)\cdot\vec{J}(\tau)\rangle d\tau, \tag{S16}$$

where k_B is the Boltzmann constant, V is the system volume, T is the temperature, τ is the correlation time, τ_0 is the integral upper limit of heat current autocorrelation function (HCACF), and the angular bracket denotes an ensemble average. Generally, the temperature in MD simulation, $T_{\rm MD}$, is calculated by the formula $\langle E\rangle = \sum_1^N \frac{1}{2}m_i v_i^2 = \frac{3}{2}Nk_B T_{\rm MD}$, where E is total kinetic energy of the group of atoms (sum of $1/2mv^2$), and N is number of total atoms. This equation is valid at high temperature.

C. Numerical results.

Numerically, the velocity Verlet algorithm is employed to integrate equations of motion, and the MD time step is set to 0.1 fs. Firstly, starting from the relaxed lattice structure using the atomic potential, the system runs in canonical ensemble (NVT) for 100 ps to equilibrate the whole system at the given temperature. Secondly, it runs in microcanonical ensemble (NVE) for 200 ps for relaxation. Lastly, it runs another 500 ps in NVE for recording the heat current at each step. The thermal conductivity is calculated using Eq. (S16). We use a combination of time and ensemble sampling to obtain better average statistics. The results represent averages from 5 independent simulations with different initial conditions.

Figure S3 shows a typical normalized HCACF along x, y, and z directions in our MD

simulations. The simulation cell is $4 \times 6 \times 4$ MD unit cells ($13.4 \times 2.3 \times 4.4$ nm^3), and the temperature is 300 K. From these data, the thermal conductivity was calculated and shown in Fig. S4. Due to the short relaxation time, the heat current autocorrelation curves decay rapidly to zero within a few picoseconds. Afterwards, the noise is comparable to the signal. Although the values of thermal conductivity along three directions (Fig. S4) are similar and not sensitive to the directions, there are differences in mechanisms. There is obvious negative autocorrelation of heat flux along x and z directions after about 0.02 ps, corresponding to a deduction in thermal conductivity. It comes from the strong reflection of flux at the molecular interfaces, which is weak along y direction, close to the π-π stacking direction.

Shown in Fig. S5, we calculated the thermal conductivity of BDTMC using different size of simulation cell. There is finite size effect when the simulation cell is smaller than $2 \times 4 \times 2$ unit cells. That is, the value of thermal conductivity increases with the simulation cell size. However, it converges when the simulation cell size is larger than $2 \times 4 \times 2$. For the data shown in Fig. 3, we used a simulation cell of $4 \times 6 \times 4$ to ensure the convergence.

IV. Additional supporting figures

Figure S6 shows the dependence of ZT on T in a larger temperature range, to show that ZT saturates at certain temperature.

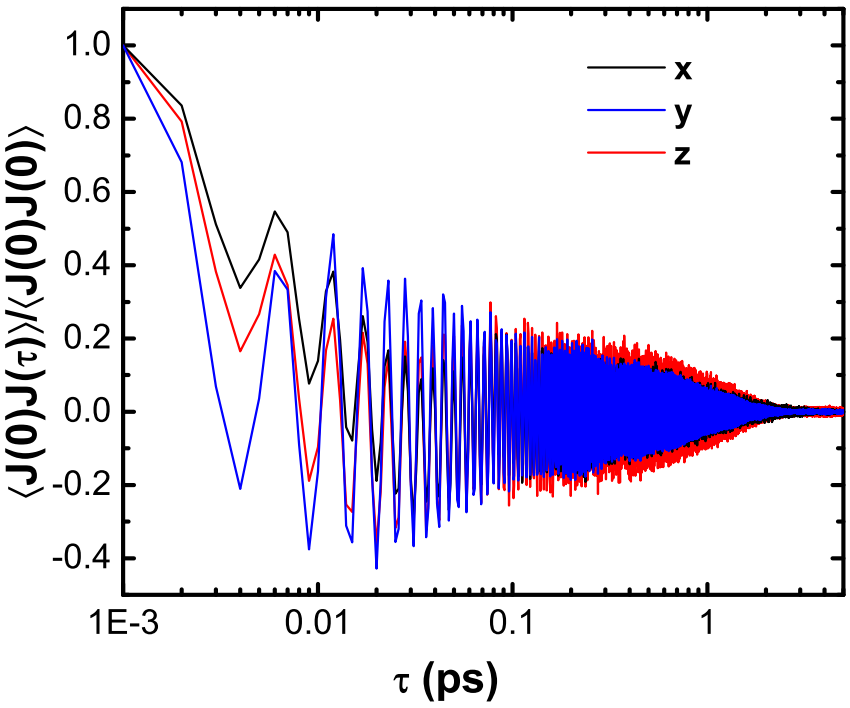

Figure S3: Normalized heat current autocorrelation function (HCACF) along x, y, and z directions.

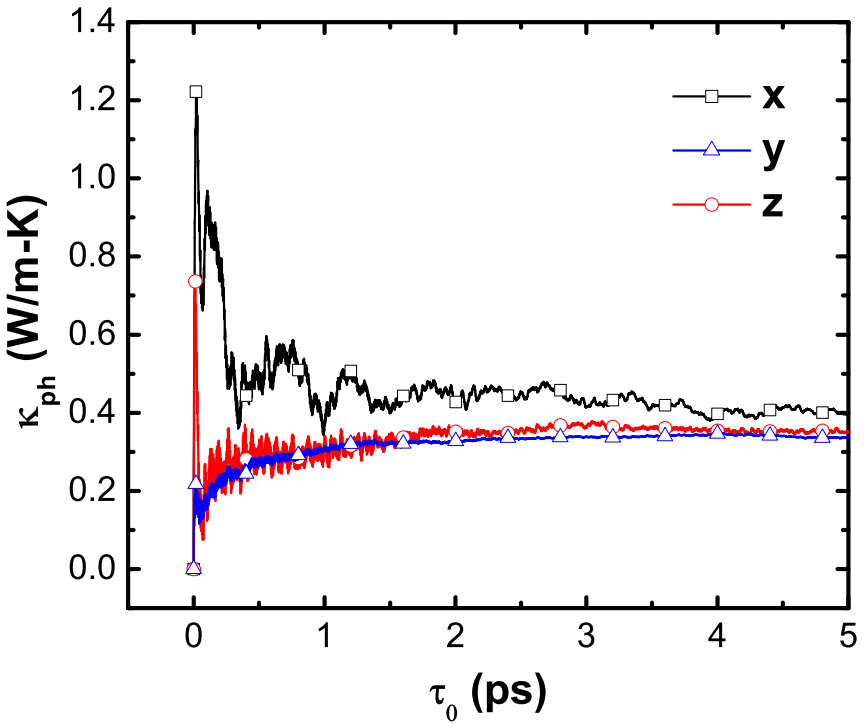

Figure S4: The phonon thermal conductivity along x, y, and z directions.

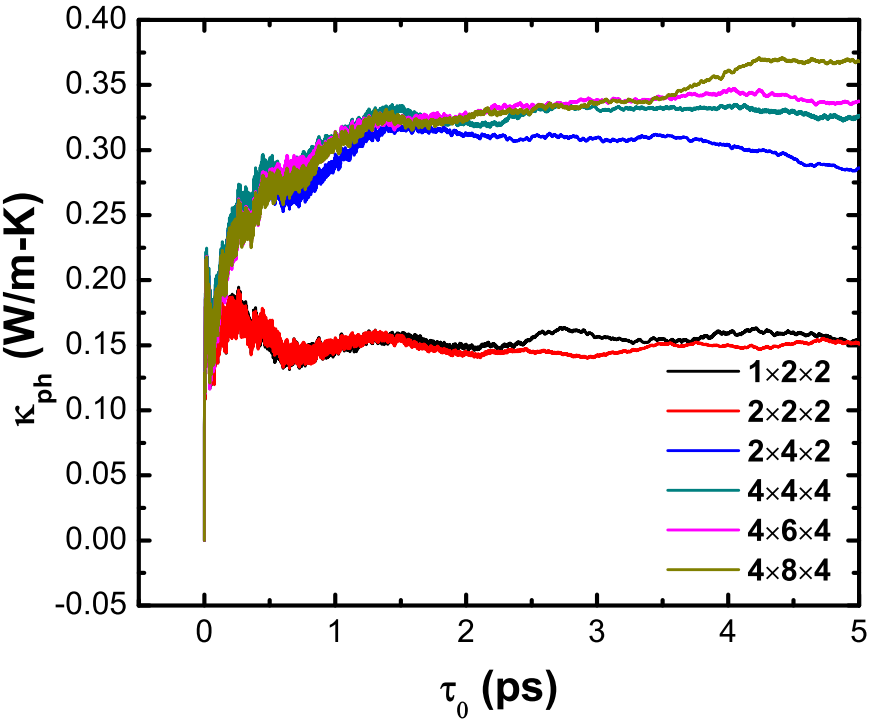

Figure S5: The phonon thermal conductivity along y direction for simulation cell with different size. The simulation cell of $1 \times 1 \times 1$ is $3.35 \times 0.38 \times 1.09$ nm^3.

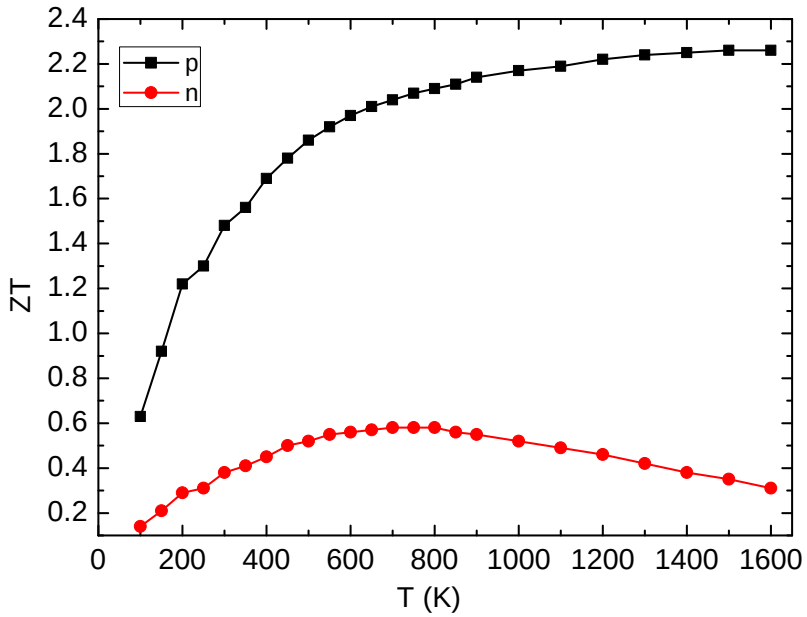

Figure S6: ZT as a function of T in a larger temperature range to show the saturation of ZT. Since using band-like transport model to model organic crystals at high temperature is questionable, we only show the result between $100 - 350$ K in the main text.

References

(1) Kresse, G.; Furthmller, J. *Comp. Mater. Sci.* **1996**, *6*, 15–50.

(2) Perdew, J.; Burke, K.; Ernzerhof, M. *Phys. Rev. Lett.* **1996**, *77*, 3865–3868.

(3) Grimme, S. *J. Comput. Chem.* **2004**, *25*, 1463–1473.

(4) Madsen, G. K. H.; Singh, D. J. *Comput. Phys. Commun.* **2006**, *175*, 67–71.

(5) Giri, G.; Verploegen, E.; Mannsfeld, S. C. B.; Atahan-Evrenk, S.; Kim, D. H.; Lee, S. Y.; Becerril, H. A.; Aspuru-Guzik, A.; Toney, M. F.; Bao, Z. *Nature* **2011**, *480*, 504–508.

(6) Bardeen, J.; Shockley, W. *Phys. Rev.* **1950**, *80*, 72–80.

(7) Beleznay, F. B.; Bogr, F.; Ladik, J. *J. Chem. Phys.* **2003**, *119*, 5690–5695.

(8) Cornell, W. D.; Cieplak, P.; Bayly, C. I.; Gould, I. R.; Merz, K. M.; Ferguson, D. M.; Spellmeyer, D. C.; Fox, T.; Caldwell, J. W.; Kollman, P. A. *J. Am. Chem. Soc.* **1995**, *117*, 5179–5197.